European Journal of Mechanics B/Fluids 30 (2011) 325–340

Contents lists available at ScienceDirect

European Journal of Mechanics B/Fluids

journal homepage: www.elsevier.com/locate/ejmflu

On the performance of linear and nonlinear k–ε turbulence models in various jet flow applications

A. Balabel, W.A. El-Askary *

Faculty of Engineering, Menoufiya University, Shebin Elkom, Menoufiya, Egypt

ARTICLE INFO

Article history:
Received 15 June 2010
Received in revised form
11 October 2010
Accepted 15 October 2010
Available online 26 October 2010

Keywords:
Numerical simulation
Two-equation turbulence models
Nonlinear turbulence model
Free jet
Impinging jet
Turbulent wall jet

ABSTRACT

In this paper, a thorough numerical investigation of the performance of several linear and nonlinear k–ε turbulence model variants in various jet flow applications is carried out. Three k–ε based turbulence models are considered, namely the standard k–ε model, the υ^2–f model, and the nonlinear k–ε model. The selected turbulence models are applied for the prediction of simple as well as complex jet flow applications to underpin knowledge about the accuracy obtained from the two-equation turbulence models. The numerical code developed by the present authors solves the unsteady RANS equations by using the control volume approach on a non-staggered grid system. Three jet flow applications are selected, namely a turbulent free jet, a turbulent jet impinging on a flat plate, and a turbulent wall jet. In order to validate the numerical results obtained and to investigate the performance of the different turbulence models considered, different experimental measurements from the literature are used. The present work is primarily motivated by the desire to provide a rational way for deciding how complex the turbulence model is required to be for a given application and to find out how the accuracy changes with model complexity. Due to the superior predictive performance of modern turbulence models in a wide range of complex industrial and engineering applications, it was believed that a 'universal' turbulence model might exist. In general, that is not true. Simple flows can be analysed using standard two-equation models. The present numerical investigation showed that the linear turbulence model could give good results in simple (non-impinging) jet flows. However, in complicated flows, such as impinging jet problems or wall jet flows, a more elaborate level of modeling is required. In such contexts, nonlinear models are appropriate for predicting the turbulent viscosity structure, namely the inhomogeneous near-wall flow region and the anisotropic Reynolds stresses, which is a vital part of turbulent jet flow prediction.

1. Introduction

Turbulent jet flows have a large number of practical applications such as entrainment and mixing processes in boiler and gas turbine combustion chambers. Also, turbulent jet flow is of central importance to many industrial and engineering applications, e.g. the aerospace industry, spray processes, internal combustion engines, agriculture and many other applications in medicine and meteorology. Despite great efforts by research engineers and scientists, turbulent flow, in general, is not well understood, and it remains an unsolved problem in fluid dynamics [1]. Only slowly have the experimental techniques become available for observing the actual jet flow structure during the last stages of evolution. However, despite recent progress in laser techniques, it is difficult to design an experiment to make the full evolution of the jet leading up to the final stages completely reproducible. Moreover, reliable quantitative data are not available. Therefore, accurate numerical simulations of the nonlinear equations have become an important tool in such areas, and they can be used to validate the theoretical models. This, together with the superior variability in the numerical simulations in the choice of fluid parameters and initial conditions, is bound to make simulations an important source of information.

The main goal in turbulence research is to obtain the velocity field as a function of space and time for a specific turbulent flow and also to derive scalar fields of some flow property of interest. Due to the difficulties in performing and comparing experiments, a numerical simulation of the problem would have been an ideal candidate for quantifying the effect of the parameters of interest. In general, turbulent flows are computed either by solving the Reynolds-averaged Navier–Stokes equations with appropriate turbulence models for modeling turbulent fluxes or by computing the fluctuating quantities directly. Indeed, it is often concluded that turbulence modeling and simulations are the factors that have set the pace for the rate of progress of computational fluid dynamics

* Corresponding author. Tel.: +20 105255817.
E-mail addresses: ashrafbalabel@yahoo.com (A. Balabel), wageeh_elaskary@yahoo.com (W.A. El-Askary).

0997-7546/$ – see front matter © 2010 Elsevier Masson SAS. All rights reserved.
doi:10.1016/j.euromechflu.2010.10.006

Nomenclature

D	Exit diameter of the jet nozzle
$dr_{1/2}/dx$	Spreading rate of jet
f	Elliptic relaxation function
H	Space distance between the jet and the impinging plate
k	Turbulence kinetic energy
L	Turbulent length scale
P_k	Production of the turbulence kinetic energy
P_{stag}	Stagnation pressure value
p	Pressure
p_c	Pressure correction
r	Radial distance from the jet centerline
$r_{1/2}$	The local jet half-width
S_{ij}	Main strain tensor, $S_{ij} = \left(\frac{\partial u_i}{\partial x_j} + \frac{\partial u_j}{\partial x_i}\right)$
T	Turbulent time scale
t	Time
t^*	Non-dimensional time, $t^* = t \times U_b/H$
U_b	Average streamwise velocity at nozzle exit
U_m	Time-averaged/mean local streamwise velocity
U_c	Time-averaged centerline velocity
uu, vv, uv	Streamwise, normal, and shear Reynolds stresses, respectively
u_τ	Friction velocity, $u_\tau = \sqrt{\tau_w/\rho}$
x, y	Coordinates in streamwise and transverse direction, respectively
y^+	Non-dimensional inner coordinate, $y^+ = u_\tau y/\nu$
y	Distance measured from the wall

Greek symbols

ε	Turbulence-energy dissipation rate
δ_{ij}	Kronecker delta ($\delta_{ij} = 1$ if $i = j$, and $\delta_{ij} = 0$ otherwise)
κ	von Kármán constant (=0.41)
μ	Laminar viscosity
μ_t	Turbulent viscosity
ν	Kinematic viscosity, $\nu = \mu/\rho$
ν_t	Turbulent kinematic viscosity, $\nu_t = \mu_t/\rho$
ρ	Fluid density
τ_w	(Time-averaged) wall shear stress
Ω_{ij}	Main vorticity tensor, $\Omega_{ij} = \left(\frac{\partial u_i}{\partial x_j} - \frac{\partial u_j}{\partial x_i}\right)$

Subscripts

c	Centerline value
i, j, k	Component i, j, k of a vector
m	Local time mean
max	Maximum value
p	Near-wall point
w	Wall condition

Acronyms

DES	Detached-eddy simulation
DNS	Direct-numerical simulation
LDA	Laser-doppler anemometer
LES	Large-eddy simulation
LEVM	Linear eddy viscosity model
NLEVM	Nonlinear eddy viscosity model
RANS	Reynolds-averaged Navier–Stokes
SHW	Stationary hot wire
SWF	Standard wall function

(CFD) in fluid engineering. This is reflected by the enormous amount of research on turbulence predictions over the past three decades. The major difficulty with turbulent flow is that it has a very wide range of length and time scales and high-frequency fluctuations embedded, which means that the equations governing turbulent flow are usually much more difficult and expensive to solve.

In general, the numerical predictions of turbulent flows have been limited in accuracy partly by the performance of three key elements, namely grid generation, algorithm development, and turbulence modeling. It is known that a well-constructed grid and a well-designed algorithm greatly improve the quality of the solution; conversely, poorly constructed grids and poorly designed algorithms are major contributors to poor results. In addition, numerical simulation difficulties such as the lack of convergence to a desired level are often a consequence of the poor grid quality or an invalid algorithm. However, the turbulence model accuracy has a large influence on the prediction of the physical phenomena encountered. Consequently, turbulence modeling has a decisive influence on drag, species transport, heat transfer, vorticity distribution, and separation. The challenging problem of turbulence modeling is how to capture the wide range of length and time scales encountered in such complex flows. Consequently, new concepts and hypotheses are continually being introduced.

Generally, three levels of modeling are commonly adopted in turbulent flow simulations. (i) Reynolds-averaged Navier–Stokes simulation (RANS) with the linear eddy viscosity model (LEVM) based on the Boussinesq assumption or with the Reynolds stress transport model (RSTM) with the six components of the Reynolds stress defined by their transport equations. (ii) The so-called large-eddy simulation (LES), where 'slowly varying' components are assumed to extend down to the mesh size where sub-grid models, based on the eddy viscosity concept, are applied. (iii) Direct numerical simulation (DNS), in which the simulations need a huge amount of computer memory, because of the grid required for computation; hence it is restricted for low Reynolds number flow simulation cases. In all approaches, there are obvious limitations and different weakness. However, the eddy viscosity concept has been remarkably successful for simple boundary layer flows and in the accurate definition of the mean flow properties for the attached unsteady boundary layer [2]. In the case of separated flows, the capabilities of different turbulence models are less certain. The LES approach is probably realistic away from a solid boundary, but near to a boundary it has all the limitations of a simple eddy viscosity model. In addition, LES and DNS are three-dimensional studies, and hence are very computationally demanding. In conclusion, DNS is presently too costly for most engineering flows. LES, although presently capable of depicting more complex flows than DNS, is still too cost intensive and not yet suitable for complex engineering problem solutions. However, recent developments in computational resources might make LES feasible for practical applications.

Recently, hybrid RANS/LES models have been developed to benefit from the computational economy of RANS but to give the higher fidelity of LES in regions of interest. Detached-eddy simulation (DES) is the original prescription for the hybrid RANS/LES solution strategies that underlie most recent work [3]. However, DES still represents many unresolved modeling issues that motivated the future work to focus on improvement of predicting different complex turbulent flow and, in addition, grid-resolution studies are necessary.

Another group of models has utilized a new methodology for simulating turbulent flows called SCALES [4], which stands for stochastic coherent adaptive large-eddy simulation. Although SCALES can outperform classical LES in different complex geometries turbulent flows at high Reynolds numbers, a local SGS model and efficient data structures are required to realize the benefits of SCALES in such highly non-homogenous flows [4].

The RSTM offers the potential for far more reliable turbulence production [5]. This is because important production terms are calculated directly from resolved variables, while the production terms of two-equation models are modeled. However, the main difficulties in the RSTM are the modeling of pressure–strain terms and the near-wall turbulence. Moreover, the numerical stability is often problematic, as a small time step is required for stability. Consequently, the RSTM is also numerically challenging and computationally expensive. All these characteristics of the RSTM are regarded as important limitations in the context of industrial CFD. This has thus motivated efforts to improve the LEVM or to construct models which combine the simplicity of eddy viscosity formulation with the superior fundamental strength and predictive properties of second-moment closure. These efforts have given rise to the group of modified LEVMs and the group of nonlinear eddy viscosity models (NLEVMs).

Two-equation models are complete in the sense that they employ two transport equations for the two turbulent scales, namely the velocity and length scales. Some improvements of the LEVM are carried out by introducing *ad hoc* corrections, usually to the length-scale equation, and/or the formulation of alternative equations for different length-scale parameters (e.g. dissipation rate ε, vorticity ω, time scale ω^{-1}). However, none of these addresses the fundamental limitations arising from the unrealistic constitutive relations, and in addition these approaches are also known to be afflicted by major weaknesses.

Among several LEVMs, the standard (STD) k–ε turbulence model [6] is still the most widely used in industrial and engineering applications, as it represents a good comparison between accuracy and computational efficiency. It was developed, calibrated, and validated to cover a wide range of industrial and engineering applications. It is a robust two-equation turbulence model and it yields quite reasonable results in high Reynolds number flow when its restrictions are considered [7]. Therefore, the two-equation STD k–ε model has been the subject of much research in recent years, even though it fails to predict a number of complex flows correctly. In particular, the two-equation STD k–ε model has limitations when the cross-sectional flow area changes or with the impinging problem. Consequently, there is a need to improve the predictions of the STD k–ε model in such applications. Recently, the development procedure has focused attention on extending the validity of the STD k–ε model in order to provide a wider range of problems with a quality turbulent flow solution at an equivalent cost.

The recent novel attempts to improve the LEVM focus on near-wall modeling and the nonlinear constitutive relation used in the nonlinear models. The near-wall modeling needs the development of low Reynolds stress transport models. The basic idea is based on the implementation of the near-wall viscous effects by damping the turbulent viscosity toward a wall by introducing a damping function. Many versions of such models can be found in [8]. The low Reynolds number k–ε model [8] dramatically overpredicts the heat transfer at the stagnation points. In more recent research [9], it is concluded that low Reynolds stress transport models are critical for heat transfer predictions. Therefore, standard k–ε turbulence modeling with its improved low Reynolds number form has been limited to specified applications or combined with other high Reynolds number models as a part of the turbulence modeling near walls.

Some improvements of the STD k–ε model have been recently developed [10]. The development was carried out either through modifying the model constants for the application of a free jet, e.g. [11] using the experimental measurements of [12], or through re-evaluation of the RNG k–ε model's constants [13] or by introducing an *ad hoc* damping function, e.g. the low Reynolds number k–ε model [14]. These modifications are adjusted to make the model fit experimental or computational data [15]. Nevertheless, no pretence has been made that any of these models can be applied to all turbulent flows: such a 'universal' model may not exist. Each model has its advantages and disadvantages, limitations, and appropriate flow regimes. One of the most important controllers of turbulence model performance is the estimated values of the model coefficients, which can be only evaluated by advanced experimental measurements over a wide range of fluid dynamics and heat transfer applications.

An alternative route is used for improving the STD k–ε model near solid boundaries through the evolution of suitable velocity and time scales of turbulence. It was noted that the unacceptable results obtained by the STD k–ε model when it is integrated to solid boundaries are due to the assignment of k as a velocity scale [16]. This and other considerations motivated the so-called υ^2–f model [17,18]. In this model, the appropriate velocity scale for turbulent transport toward the wall is the velocity fluctuation normal to streamlines υ^2, thereby introducing the effects of streamline curvature in a natural way. Moreover, the υ^2–f model formula provides the right scaling in representing the damping of transport close to the wall.

The υ^2–f model was originally developed for attached or mildly separated boundary layers. Recently, it was also applied in examples of massive separation and unsteady vortex shedding [18]. The starting point of the υ^2–f model is the Boussinesq assumption as well as any other linear eddy viscosity model, i.e. the overall effect on the mean flow is completely isotropic. Therefore, more recently, a number of modifications have been introduced in order to derive a non-isotropic relationship for the normal Reynolds stresses. These efforts have given rise to the group of nonlinear eddy viscosity models in more complex engineering applications [19].

The most important defects of the LEVM are the modeling of the Reynolds stresses using the linear Boussinesq stress–strain relations. This gives a wholly unrealistic representation of normal stress anisotropy, observed in virtually all shear flows, and the substantial errors in complex strain, in which the gradients of the normal stresses contribute significantly to the momentum balance. Other predictive deficiencies include incorrect sensitivity to curvature strain and dilation, excessive levels of turbulence in regions of strong normal straining, wrong response to swirl, and the suppression of self-induced periodic motions.

To avoid the related problems of the LEVM, an alternative route thus pursued recently has been nonlinear eddy viscosity models (NLEVMs) [20,21]. This approach is based on the nonlinear extension of the linear stress–strain relation. Consequently, the Reynolds stresses are defined by an algebraic formula depending on a nonlinear combination of mean strain and vorticity as well as k and ε. In this way, some of the weaknesses of the LEVM related to turbulence production near stagnation, insensitivity to curvature, flow separation on curved surfaces, and often poor predictions of transitions are avoided, and the well-defined important effects are represented.

The NLEVM is an important topic in recent modeling of turbulent flow. This approach has been developed to describe the flow in a more physically consistent manner. The NLEVMs are made to mimic the physics of turbulence by means of mathematical artifacts and calibration, and, in addition, they provide a mechanism for anisotropy of the normal stresses. The basic idea of the NLEVM is the extension of the original linear stress–strain relation to a nonlinear form. Consequently, the Reynolds stresses are defined by algebraic formulae depending on a nonlinear combination of mean strain and vorticity as well as k and ε, with coefficients which may be tuned for particular applications. The NLEVM's performance was tested in our previous research [21] on asymmetric divergent channel flow, and good results were obtained.

Most NLEVMs are usually quadratic or cubic according to the order of the characteristic time scale $\tau = k/\varepsilon$ in the anisotropy

tensor equation. These differences in order are of considerable significance. In particular, cubic models play an essential role in capturing the strong effects of curvature on the Reynolds stresses. The comparison of many quadratic stress–strain relations with experimental data showed that none achieves much greater width of applicability. However, the model of Craft et al. [19] has proposed a cubic relation between the strain and vorticity tensor and the stress tensor; this did much better than conventional eddy viscosity models in capturing the streamline curvature and the anisotropic stresses over a wide range of flows.

In the present paper, the STD k–ε model, the v^2–f model, and the nonlinear k–ε (cubic model) are investigated against three jet flow problems, namely a free round jet, a jet impinging on a flat plate, and a turbulent wall jet. The solution quality obtained from the different assorted formulations of two-equation turbulence models is discussed in detail. Moreover, a number of different criteria which are used to judge the turbulence model performance are explored.

The sections below give details of the governing equations, the different turbulence modeling strategies, and the numerical approaches adopted. Further, the cases studied are explained in detail and the present numerical results obtained are compared with different techniques of experimental measurements. Finally, conclusions are drawn.

2. Computational methodology

2.1. The governing equations

Starting from the continuity and momentum equations for unsteady, two-dimensional, incompressible, and Newtonian flow, and following the Reynolds-averaged procedure, where the instantaneous variables for the velocity and pressure field are decomposed into the mean and fluctuating components, one obtains the so-called Reynolds-averaged Navier–Stokes (RANS) equations. In tensor notation, the RANS equation can be written in time-accurate form as follows:

$$\frac{\partial}{r^\alpha \partial x_i}(r^\alpha \rho u_i) = 0 \tag{1}$$

$$\frac{\partial}{\partial t}(\rho u_i) + \frac{\partial}{r^\alpha \partial x_j}(r^\alpha \rho u_i u_j) = -\frac{\partial p}{\partial x_i} + \frac{\partial r^\alpha}{r^\alpha \partial x_j}\left[\mu\left(\frac{\partial u_i}{\partial x_j} + \frac{\partial u_j}{\partial x_i}\right) + (-\rho\overline{u_i' u_j'})\right], \tag{2}$$

where $a = 0$ or 1 for two-dimensional flow (x–y coordinates) or axisymmetric flow (x–r coordinates), respectively, ρ is the fluid density, μ is the dynamic viscosity, u_i and u_j denote ensemble-average quantities, u' is a fluctuating or turbulence quantity, and p is the pressure. The quantities $-\rho\overline{u_i' u_j'}$ are known as Reynolds stresses. In order to close the above equations, turbulence models are needed to model the apparent Reynolds stresses. For the LEVM, the linear stress–strain relation is assumed to follow the Boussinesq assumption:

$$-\rho\overline{u_i' u_j'} = \mu_t\left(\frac{\partial u_i}{\partial x_j} + \frac{\partial u_j}{\partial x_i}\right) - \frac{2}{3}\rho k \delta_{ij}, \tag{3}$$

where δ_{ij} is the Kronecker delta function ($\delta_{ij} = 1$ if $i = j$ and $\delta_{ij} = 0$ if $i \neq j$), k is the turbulent kinetic energy, and μ_t is the turbulent viscosity.

2.2. Two-equation turbulence models

Until recent years, two-equation turbulence models served as the foundation for much of the turbulence model research. Two-equation models are complete in the sense that they employ two transport equations for the two turbulent scales, namely the velocity and length scales. The starting point of all two-equation models is the Boussinesq constitutive relation and the turbulent kinetic energy equation. Apart from that, a second transport equation is solved to determine the length scale.

2.2.1. The standard k–ε model (STD k–ε)

The k–ε model is one of the most popular two-equation turbulence models in CFD. The most commonly used formulation of the k–ε turbulence model is known as the standard k–ε model, which was developed by [3]. In the standard formulation of the k–ε model, two transport equations for the turbulent kinetic energy k and its dissipation rate ε are specified:

$$\frac{\partial}{\partial t}(\rho k) + \frac{\partial}{r^\alpha \partial x_j}(r^\alpha \rho u_j k) = \frac{\partial}{r^\alpha \partial x_j} r^\alpha \left[\left(\mu + \frac{\mu_t}{\sigma_k}\right)\frac{\partial k}{\partial x_j}\right] + \rho(P_k - \varepsilon) \tag{4}$$

$$\frac{\partial}{\partial t}(\rho \varepsilon) + \frac{\partial}{r^\alpha \partial x_j}(r^\alpha \rho u_j \varepsilon) = \frac{\partial}{r^\alpha \partial x_j} r^\alpha \left[\left(\mu + \frac{\mu_t}{\sigma_\varepsilon}\right)\frac{\partial \varepsilon}{\partial x_j}\right] + \rho(C_{1\varepsilon} P_k - C_{2\varepsilon}\varepsilon)\frac{\varepsilon}{k}. \tag{5}$$

The turbulent kinetic energy production rate is defined as

$$P_k = \nu_t\left(\frac{\partial u_i}{\partial x_j} + \frac{\partial u_j}{\partial x_i}\right)\frac{\partial u_i}{\partial x_j}, \tag{6}$$

where ν_t is defined as μ_t/ρ, and the turbulent viscosity μ_t is defined as

$$\mu_t = \rho C_\mu \frac{k^2}{\varepsilon}. \tag{7}$$

The standard values of the empirical constants are

$$C_\mu = 0.09, \quad \sigma_k = 1, \quad \sigma_\varepsilon = 1.3, \quad C_{1\varepsilon} = 1.44, \quad C_{2\varepsilon} = 1.92.$$

In simulations with the STD $k - \varepsilon$ model, one significant problem with an impinging jet (one of the cases studied here) is the handling of the near-wall, viscosity-affected layer. A full resolution of this, with a low Reynolds number turbulence model, is very expensive, as a result of the extremely fine grid needed. Hence the present work has used the wall function to approximate the flow development across this layer, allowing the use of a coarser near-wall grid, with the first near-wall node ideally placed outside the viscous layer, in the fully turbulent region of the flow. Standard forms of wall functions (SWFs) are based on an assumed logarithmic mean velocity profile and local equilibrium conditions, leading to the near-wall velocity profile being given in non-dimensional form as $U^+ = \frac{1}{\kappa} Ln(E_f y^+)$, where $E_f = 9.8$ for smooth walls as assumed in the present work, $\kappa = 0.41$ is the von Kármán constant, $U^+ = \rho U k_p^{1/2}/\tau_w$, and $y^+ = \frac{y k_p^{1/2}}{\nu}$, with τ_w the wall shear stress, y the distance from the wall, and k_p the turbulent kinetic energy at the near-wall node. At the wall, the boundary value for the dissipation rate at the first near-wall point (identified by the subscript p) can be expressed as $\varepsilon_p = \frac{C_\mu^{0.75} k_p^{1.5}}{\kappa y_p}$. The near-wall value of the turbulence kinetic energy k is computed by solving the complete transport equation for k in the near-wall control volume, with the wall shear stress included in the production term and zero normal gradients assumed for k at the wall.

2.2.2. The v^2–f model

The v^2–f model was introduced as a restriction of a full second-moment closure model [17]. It is able to predict the damping of turbulence transport near solid boundaries accurately without using either wall functions or damping functions. In addition, it can

reproduce the well-known near-wall non-local effects of pressure deformation fluctuations. The v^2–f model including its variants has been validated over a wide range of complex flows [22].

In the v^2–f model, two additional transport equations for v^2 and f are solved along with the STD k–ε equations (Eqs. (4) and (5)). The v^2 transport equation (regarded simply as a velocity scale that satisfies the boundary conditions appropriate for the normal component of turbulent intensity) can be given as follows:

$$\frac{\partial}{\partial t}(\rho v^2) + \frac{\partial}{r^\alpha \partial x_j}(r^\alpha \rho u_j v^2) = \frac{\partial}{r^\alpha \partial x_j}\left[r^\alpha \left(\mu + \frac{\mu_t}{\sigma_k}\right)\frac{\partial v^2}{\partial x_j}\right] + \rho\left(kf - v^2\frac{k}{\varepsilon}\right). \tag{8}$$

The quantity v^2 is obtained from a transport equation simplified from second-moment closure. The associated pressure strain term, which is responsible for the redistribution of turbulence energy in the proximity of walls to return the correct level of turbulence anisotropy, is obtained by solving an auxiliary *elliptic relaxation* equation for f:

$$L^2\frac{\partial^2 f}{\partial x_j^2} - f = \frac{1}{T}\left[(C_1 - 6)\frac{v^2}{k} - \frac{2}{3}(C_1 - 1)\right] - C_2\frac{P_k}{k}, \tag{9}$$

where the turbulent time T and length scale L are given as follows:

$$T = \max\left(\frac{k}{\varepsilon}, 6\sqrt{\frac{\nu}{\varepsilon}}\right), \qquad L = C_L \max\left(\frac{k^{1.5}}{\varepsilon}, C_\eta\frac{\nu^{0.75}}{\varepsilon^{0.25}}\right), \tag{10}$$

where ν is the kinematic viscosity. Consequently, the turbulent viscosity μ_t is defined as

$$\mu_t = \rho C_\mu v^2 T. \tag{11}$$

The constants of the adopted v^2–f model are chosen following the so-called v^2–f friendly model [22]:

$$\begin{aligned} &C_\mu = 0.22, \quad \sigma_k = 1, \quad \sigma_\varepsilon = 1.3,\\ &C_{1\varepsilon} = 1.4(1 + 0.05\sqrt{k/v^2}); \quad C_{2\varepsilon} = 1.9,\\ &C_1 = 1.4; \quad C_2 = 0.3; \quad C_L = 0.23; \quad C_\eta = 70. \end{aligned} \tag{12}$$

2.2.3. The nonlinear k–ε model

The previously described models (the STD k–ε model and the v^2–f model) still follow the Boussinesq hypothesis in the definition of the stress–strain relation. The idea of nonlinear eddy viscosity models (NLEVMs) is to extend the linear constitutive relation to a nonlinear one, which would be able to capture more physics. This can be simply done by introducing some additional terms in the stress–strain relation, related to the mean strain and vorticity tensors. According to [20], the constitutive relation for a cubic NLEVM can be written as

$$\begin{aligned} \overline{u_i' u_j'} = {} & \frac{2}{3}k\delta_{ij} - 2C_\mu f_\mu \frac{k^2}{\tilde{\varepsilon}}S_{ij} + \frac{k^3}{\tilde{\varepsilon}^2}\left[C_1\left(S_{ik}S_{jk} - \frac{1}{3}S_{kl}S_{kl}\delta_{ij}\right)\right.\\ & \left. + C_2(S_{ik}\Omega_{jk} + S_{jk}\Omega_{ik}) + C_3\left(\Omega_{ik}\Omega_{jk} - \frac{1}{3}\Omega_{kl}\Omega_{kl}\delta_{ij}\right)\right]\\ & + \frac{k^4}{\tilde{\varepsilon}^3}\left[C_4(S_{ik}\Omega_{jl} + S_{jk}\Omega_{il})S_{kl}\right.\\ & \left. + C_5\left(\Omega_{ik}\Omega_{kl}S_{lj} + \Omega_{jk}\Omega_{kl}S_{li} - \frac{2}{3}\Omega_{kl}S_{lm}\Omega_{mk}\delta_{ij}\right)\right]\\ & + \frac{k^4}{\tilde{\varepsilon}^3}\left[C_6\left(S_{kl}S_{kl}S_{ij}\right) + C_7\left(\Omega_{kl}\Omega_{kl}S_{ij}\right)\right], \end{aligned} \tag{13}$$

where the main strain and vorticity tensors are defined by

$$S_{ij} = \left(\frac{\partial u_i}{\partial x_j} + \frac{\partial u_j}{\partial x_i}\right), \qquad \Omega_{ij} = \left(\frac{\partial u_i}{\partial x_j} - \frac{\partial u_j}{\partial x_i}\right). \tag{14}$$

The ε-transport equation, Eq. (5), is then modified to include low Reynolds number terms for the adequate wall treatment according to the following form:

$$\begin{aligned} &\frac{\partial}{\partial t}(\rho\tilde{\varepsilon}) + \frac{\partial}{r^\alpha \partial x_j}(r^\alpha \rho u_j \tilde{\varepsilon})\\ &\quad = \frac{\partial}{r^\alpha \partial x_j} r^\alpha\left[\left(\mu + \frac{\mu_t}{\sigma_\varepsilon}\right)\frac{\partial\tilde{\varepsilon}}{\partial x_j}\right]\\ &\qquad + \rho(C_{1\varepsilon}f_1 P_k - C_{2\varepsilon}f_2\tilde{\varepsilon})\frac{\tilde{\varepsilon}}{k} + \rho E, \end{aligned} \tag{15}$$

where the homogeneous and inhomogeneous parts of the dissipation rate are defined as follows [20]:

$$\varepsilon = \tilde{\varepsilon} + D. \tag{16}$$

The associated model constants and coefficients are described as follows [20]:

$$\begin{aligned} &C_\mu = \frac{0.3}{1 + 0.35\eta^{1.5}}(1 - \exp(-0.36\exp(0.75\eta)))\\ &\eta = \mathrm{Max}(\bar{S}, \bar{\Omega}), \qquad \bar{S} = (k/\varepsilon)\sqrt{2S_{ij}S_{ij}},\\ &\bar{\Omega} = (k/\varepsilon)\sqrt{2\Omega_{ij}\Omega_{ij}} \qquad f_\mu = 1 - \exp\left[-\left(\frac{R_t}{90}\right)^{0.5} - \left(\frac{R_t}{90}\right)^2\right],\\ &f_1 = 1, \qquad f_2 = 1 - 0.3\exp(-R_t^2) \qquad D = 2\nu\left(\frac{\partial k^{0.5}}{\partial x_i}\right)^2,\\ &R_t = \frac{k^2}{\nu\tilde{\varepsilon}}, \qquad E = 0.0022\frac{\nu_t\bar{S}k^2}{\tilde{\varepsilon}}\left(\frac{\partial^2 U_i}{\partial x_j \partial x_k}\right)^2 \Rightarrow R_t < 250\\ &C_1 = -0.4C_\mu f_\mu, \qquad C_2 = -C_1, \qquad C_3 = 1.04C_\mu f_\mu,\\ &C_4 = 80C_\mu^3 f_\mu, \qquad C_5 = 0, \qquad C_6 = -40C_\mu^3 f_\mu,\\ &C_7 = -C_6, \end{aligned}$$

where the dimensionless parameters $\bar{S}$, $\bar{\Omega}$ are known as the normalized strain and vorticity tensors. In such a context, the turbulent viscosity μ_t is then defined as

$$\mu_t = \rho C_\mu f_\mu \frac{k^2}{\tilde{\varepsilon}}. \tag{17}$$

It should be pointed out that, when $C4 = C5 = C6 = C7 = 0$, the so-called quadratic model is obtained. In our study, only the cubic model is considered.

The above-described nonlinear k–ε turbulence model is applied in the present study, and its results are compared with those obtained from the other considered linear turbulence models (the STD k–ε model and the v^2–f model). Different previous experimental data are also used for the assessment of the all adopted turbulence models in the prediction of the selected computational jet dynamics applications. The developed numerical method and procedure applied for solving the above system of equations (RANS equations and the turbulence model equations) are explained in detail in the following section.

2.3. Numerical procedure

All the dependent variables of interest here (u, v, k, ε, v^2, f) follow the generalized conservation principle. The general differential equation for unsteady, incompressible, and two-dimensional ($\alpha = 0$, $r \equiv y$) or axisymmetric ($\alpha = 1$) flow is given by

$$\frac{\partial}{\partial t}(\rho\varphi) + \frac{1}{r^\alpha}\left(\frac{\partial}{\partial x}r^\alpha(\rho u\varphi) + \frac{\partial}{\partial r}r^\alpha(\rho v\varphi)\right) = \frac{1}{r^\alpha}\left(\frac{\partial}{\partial x}\left(r^\alpha\Gamma_\varphi\frac{\partial\varphi}{\partial x}\right) + \frac{\partial}{\partial r}\left(r^\alpha\Gamma_\varphi\frac{\partial\varphi}{\partial r}\right)\right) + S_\varphi, \quad (18)$$

where φ is the dependent variable, Γ_φ is the diffusion coefficient for φ, and S_φ is the source term. The quantities Γ_φ and S_φ are specific to a particular meaning of φ. This arrangement of the governing equations is necessary for suitable application of the control volume approach proposed by [23]. The resulting governing equations presented here are discretized and solved on non-staggered, structured and cell-centred collocated grids using the implicit fractional step non-iterative method on the basis of the control volume approach [23]. The implementation of a single cell network for all variables with a collocated specification of variables at the centre of each cell requires high-order approximation for calculating the fluxes at cell faces to ensure a proper velocity–pressure coupling and to prevent the associated pressure oscillations. As there is no pressure transport equation considered, the continuity equation is satisfied by solving the Poisson equation for pressure using the successive over-relaxation method. This method is referred to as a split-step pressure correction method; it was developed and applied successfully in our previous research for single-phase and two-phase flow applications [24].

Our strategy for solving the appropriate system of equations is carried out by presuming that the velocity field reaches its final value in two stages; this means that

$$\mathbf{u}^{n+1} = \mathbf{u}^* + \mathbf{u}_c, \quad (19)$$

where $\mathbf{u}^*$ is an imperfect velocity field based on a guessed pressure field, and $\mathbf{u}_c$ is the corresponding velocity correction. First, the 'starred' velocity will result from the solution of the momentum equations. The second stage is the solution of the Poisson equation for the pressure:

$$\nabla^2 p_c = \frac{\rho}{\Delta t}\nabla\cdot\mathbf{u}^*. \quad (20)$$

where Δt is the prescribed time step and p_c is called the pressure correction. Once the Poisson equation is solved, one gets the appropriate pressure correction, and consequently, the velocity correction is obtained according to

$$\mathbf{u}_c = -\frac{\Delta t}{\rho}\nabla p_c. \quad (21)$$

After obtaining the divergence-free velocity field, the turbulence model equations are solved on the computational domain and, then, the whole solution algorithm is repeated until it reaches the statistically steady-state condition.

However, the numerical method described above has second-order accuracy in space and first-order accuracy in time. The prescribed time step is assumed to be small enough and constant to ensure a stable numerical solution; consequently, there is no need to apply CFL criteria.

3. Results and discussion

3.1. A self-preserving axisymmetric turbulent jet

Although a self-preserving axisymmetric turbulent jet is considered as a relatively simple turbulent shear flow, it represents a benchmark for research into the physics of turbulent fluid flow. The importance of the free jet to the understanding of turbulence is evidenced by the large number of publications involving experimental data, mathematical analysis, and computational modeling. Many relevant technical applications are based upon jets, e.g. rocket engines and gas turbines.

It was established that the jet was truly self-preserving some distance downstream of the nozzle, and therefore most of the results were presented in excess of this distance. However, the turbulent intensity showed marked departures from self-preservation even on the axis of the jet. Therefore, the numerical simulation of the axisymmetric turbulent jet, presented in the present paper, is used to investigate the performance of the implemented turbulence models and the developed numerical scheme. Great emphasis is placed on the prediction of the Reynolds stresses that can describe the flawless performance of the adopted turbulence models. Indeed, jets pose a difficult problem for turbulence models employing a single fixed set of constants [25]. Jets are therefore widely used as a standard test-case in turbulence modeling evaluation.

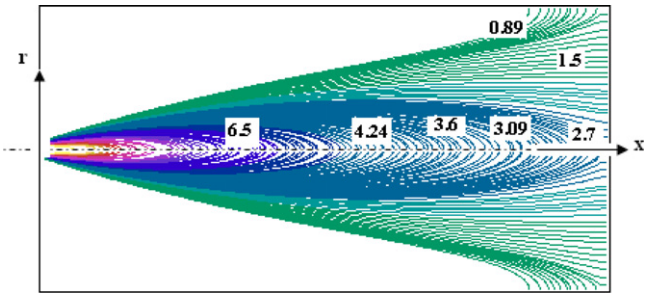

Fig. 1. Axial velocity contours for an axisymmetric turbulent jet (present simulation for Re $= 10^5$).

The axisymmetric turbulent jet simulated in the numerical experiment reported here, as shown in Fig. 1, was modified to closely match the boundary conditions of the experimental work of [26]. Air with a mean velocity of $U_m = 51$ m/s exits through a central nozzle with a diameter of $D = 26.4$ mm into ambient air at atmospheric pressure. In this case, the Reynolds number is Re $= 10^5$ and the Mach number is Ma $= 0.15$, both numbers allowing the flow to be considered incompressible. It was concluded by [27] that the effect of the initial conditions near the nozzle exit diminishes rather slowly with downstream distance; therefore the computational domain is allowed to extend more than 70 diameters downstream of the nozzle. At the nozzle exit, a uniform velocity distribution is employed. The turbulent intensity at the nozzle exit is estimated using the ratio of the turbulent fluctuating to mean velocity at the nozzle exit as $I = u'/U_m \approx 0.16\mathrm{Re}^{-0.125}$. The resulting inlet kinetic energy is $k_{\mathrm{inlet}} = 1.5(U_m I)^2$, and the corresponding dissipation rate $\varepsilon_{\mathrm{inlet}} = (C_\mu)^{0.75}(k_{\mathrm{inlet}})^{1.5}/l$, where l is the turbulent length scale, assumed to be equal to the nozzle diameter, and C_μ is a constant, equal to 0.09.

As a result of the symmetrical characteristics of the turbulent jet considered, only the upper half of the computational domain is simulated. The computational grid employed here consists of 101 (axial) by 151 (radial) grid cells for a computational domain dimension of 3 $\times$ 1.0 m^2, respectively. In fact, we performed the simulation with three different grids: 51 $\times$ 75, 101 $\times$ 151 and 203 $\times$ 303 in the axial and radial directions, respectively. No noticeable differences in the results were obtained from the finest and medium grids, while the rough grid produced unsatisfactory results compared with the experimental measurements, so we only employ here the medium grid. Four types of boundary condition were used to describe the flow field within the computational domain, namely inlet boundary conditions at the nozzle exit, axis of symmetry along the jet centerline, outlet boundary conditions at the top and the right end of the computational domain, and slip boundary conditions at the west side, see Fig. 1.

In the early experimental investigation of [26], which was carried out by using linearized constant-temperature hot-wire anemometers, the velocity of the jet was maintained constant to accuracy better than 1%, and the scatter in r.m.s. values was less than 1%.

The same experiment was repeated in [28] by using both stationary and flying hot-wire and burst-mode LDA techniques for the

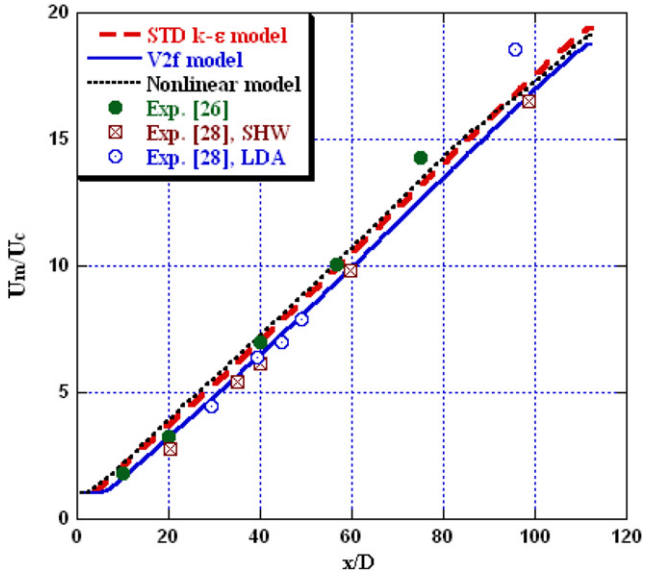

Fig. 2. Variation of the centerline axial velocity.

same source and boundary conditions. The uncertainty in the estimation of the jet exit momentum was approximately 2.6% [28]. The sampling error for obtaining the mean values using the hot-wire anemometers was approximately 3% at the outermost radial location and 0.7% at the centerline [28]. In spite of the LDA techniques applied, there was considerably more scatter in LDA results (typically 5%) than in the hot-wire measurements; see [28]. The experimental measurements presented in [28] differed substantially from those reported in [26]. These differences were attributed to the smaller enclosures used in the earlier experiment of [26] and due to the recirculation encountered within it. Moreover, the flying hot-wire and burst-mode LDA measurements presented in [28] were different from the stationary wire measurements due to the effect of the high turbulence intensity at the jet centerline on the performance of the measuring instruments [28]. According to such associated experimental discrepancies, in addition to the superior variability of simulations (in the choice of fluid parameters and of initial conditions), numerical simulations have recently become an important source of information that is not available experimentally. Therefore, the numerical results obtained in the present work are compared with the experimental measurements of [26,28].

3.1.1. Mean velocity profiles

Fig. 2 illustrates the variation of the predicted centerline velocity, normalized by the inlet mean velocity, as a function of the axial location normalized using the nozzle diameter at a distance of $x/D = 75$. The numerical results predicted by the implemented different turbulence models are compared with the experimental measurements of [26,28]. The experimental measurements of [26] were carried out by using linearized constant-temperature hot-wire anemometers, while the experimental measurements of [28] were performed by using the stationary hot-wire (SHW) technique and burst-mode laser Doppler anemometry (LDA).

Fig. 2 indicates the decay rate of the centerline velocity U_c represented by a straight line revealing the self-preserving characteristics of the jet. The greater the slope of the line, the higher the decay rate of the centerline velocity. The virtual origin of the jet is represented by the initial nearly constant part of the profile. All the turbulence models adopted predict the linear distribution of the centerline velocity well. However, the results predicted by the v^2–f model are the nearest results to the experimental measurements made by using the SHW technique regarding the prediction of the virtual origin of the jet, $x/D \approx 4.5$, which is in close agreement

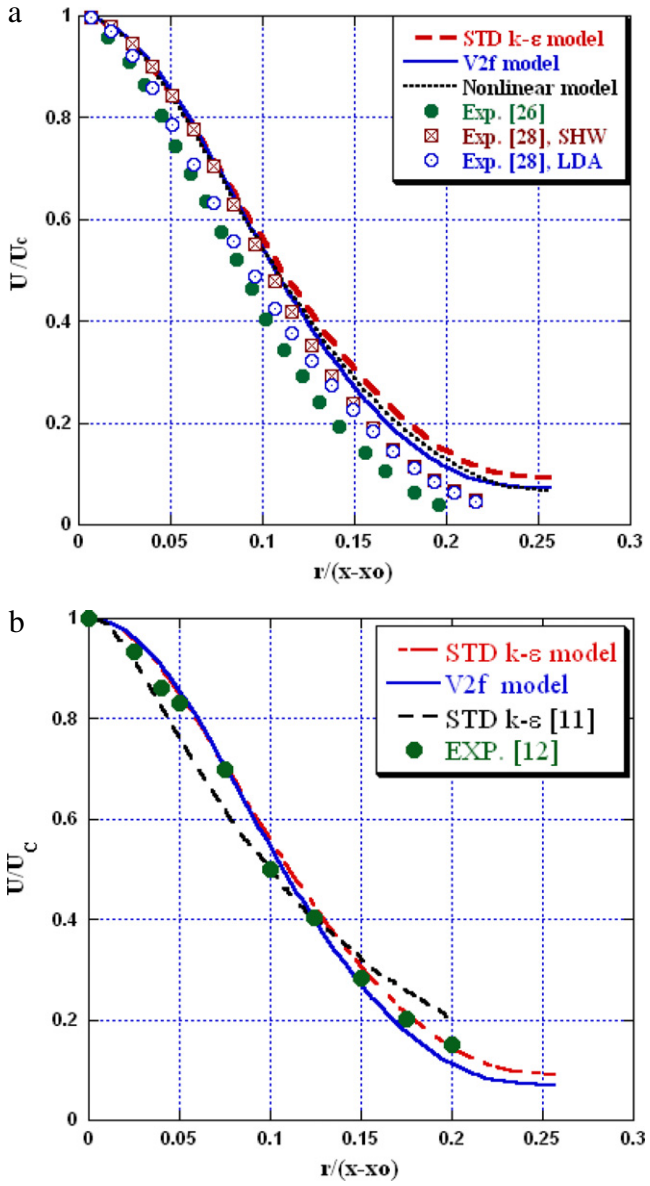

Fig. 3. Mean axial velocity profile in the radial direction at $x/D = 75$, compared with previous experimental measurements (a) and previous RANS simulation (b).

with the prediction of [28] ($x/D \approx 4.0$), while $x/D \approx 7.0$ is reported in the experiment of [26]. The predicted values of the virtual origin using the STD model or the nonlinear model are $x/D \approx 2.3$ and 3.2, respectively. These results indicate that the v^2–f model is capable of predicting the virtual origin of the jet correctly.

Fig. 3(a) shows the axial velocity distribution in the radial direction, normalized by the centerline velocity and plotted versus the non-dimensional radial coordinates at an axial location of $x/D = 75$. The numerical results predicted by the different turbulence models adopted are compared with the experimental measurements of [26,28]. The three turbulence models adopted give almost coincident profiles. The variation in the three predicted velocity profiles occurs only in the outer portion of the jet ($r/(x - xo) > 0.15$), with a close prediction of the v^2–f model to the experimental measurements. However, these differences could not be considered significant in the prediction of the radial distribution of the streamwise velocity as the difference between the v^2–f model and the nonlinear model is very small.

In order to show the accuracy of the present RANS simulation, another validation is carried out in Fig. 3(b) by comparing

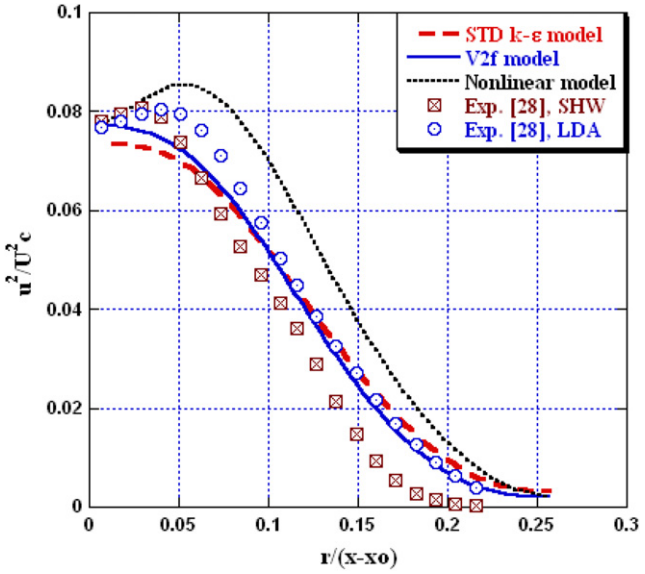

Fig. 4. Streamwise component of the Reynolds stresses at $x/D = 75$.

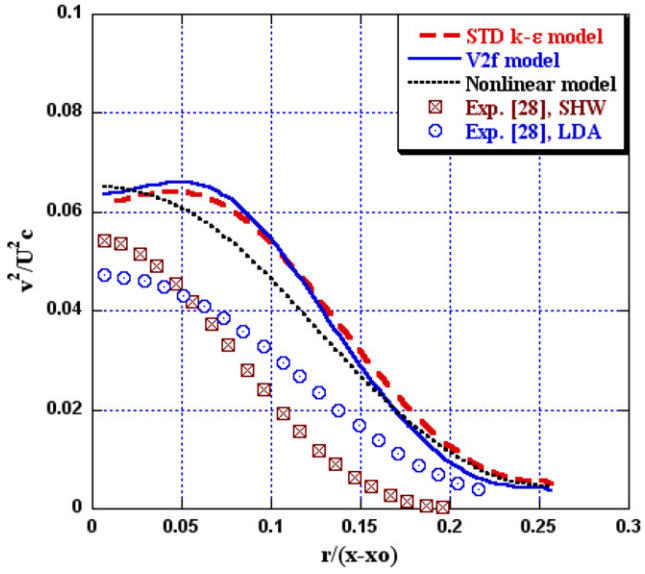

Fig. 5. Normal component of the Reynolds stresses at $x/D = 75$.

the numerical results obtained from the linear models (STD k–ε and v^2–f models) with the previous RANS simulation of [11] using the STD k–ε model and with the same experimental measurements of [12], considered in [11] for numerical results verification. Fig. 3(b) shows that the present RANS results are in better agreement with the experimental measurements of [12] than those of [11]. This could be a consequence of the numerical scheme adopted in the present paper.

It should be pointed out that the differences between the experimental measurements of both [26] and [28] are an consequence of the experimental facilities used in [28], while the discrepancies between the two experimental techniques (SHW and LDA) are small but have non-negligible effects. Therefore, the comparison of the numerical results with the experimental measurements of [28] is worthwhile. Consequently, we restrict the verification of the turbulence models to the comparison of the Reynolds stresses in the experimental measurements of [28].

3.1.2. *Reynolds stresses (second moments of velocity)*

The Reynolds stresses in both the streamwise and normal directions are non-dimensionalized by the square of the centerline velocity and compared, for all turbulence models adopted, with the experimental measurements of [28], as shown in Figs. 4 and 5.

The streamwise component of the Reynolds stresses is plotted in Fig. 4. The numerical results obtained from the STD k–ε and the v^2–f models show better agreement with the LDA data than those predicted by the nonlinear model, which overpredicts the experimental measurements. This can be attributed to the excessive prediction of the normal stresses by the nonlinear models in such cases where the anisotropic stress effects have a smaller contribution to the Reynolds stresses. The prediction of the normal component of the turbulent Reynolds stresses is shown in Fig. 5, where all turbulence models overpredict the experimental measurements. This might be attributed to the effect of the leading cross-flow error on the measuring instruments [28]. In general, the STD k–ε model and the v^2–f model showed nearly the same distribution. However, the nonlinear model showed a different profile.

The turbulent shear stress is plotted in Fig. 6. All the turbulence models adopted in the present paper showed an overall qualitative agreement with the LDA measurements, while the SHW measurements failed to predict the distribution of the turbulent shear stresses. A fairly quantitative agreement has been obtained for

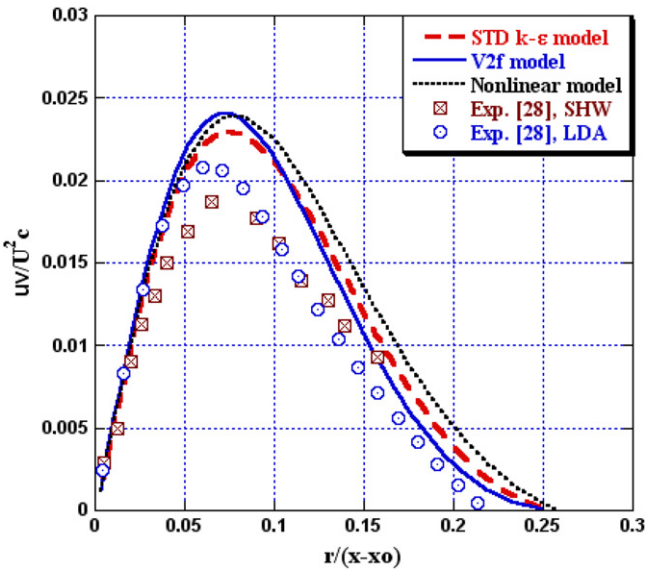

Fig. 6. Turbulent shear stress for an axial free jet at $x/D = 75$.

the STD k–ε and v^2–f models. However, the nonlinear model still overpredicts the experimental measurements. This may be a consequence of the nonlinear constitutive relations presented in the nonlinear model and the model constants included. The results obtained from the nonlinear turbulence model are clearly affected by the constant values which were previously calibrated in the original paper of [19] to give the best agreement with the experimental measurements only in the case of the impinging-jet problem.

In general, and from the previous comparisons, it can be concluded that linear models such as the STD k–ε and v^2–f models are better than nonlinear models in the prediction of simple turbulent shear flows. In such cases, the nonlinear model, as a result of its nonlinear constitutive relation, overpredicts the normal Reynolds stresses in comparison with the experimental measurements or the other linear turbulence models. The nonlinear model might be useful in other jet applications where the anisotropic stresses have a large contribution to the Reynolds stress predictions. Some important jet applications are the jet impinging and wall jet problems, which are described in the following sections.

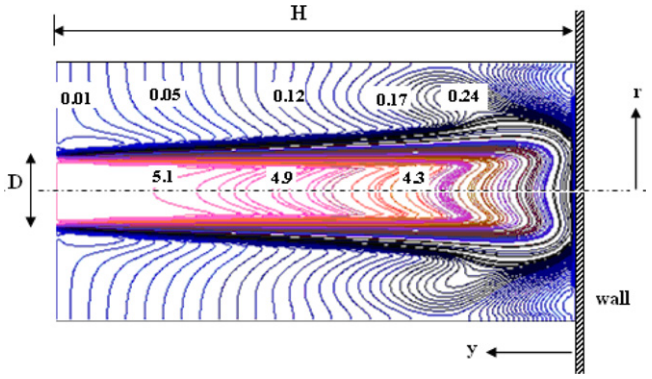

Fig. 7. Axial velocity contours for the impinging jet problem (present simulation, for $H/D = 2$ at Re = 23 000).

3.1.3. Jet spreading rate

One of the important characteristic variables of round turbulent jets is their spreading rate $dr_{1/2}/dx$. The jet half-width $r_{1/2}$ is defined as the radial distance from the jet axis to the point at which the local mean axial velocity is half the mean axial velocity on the jet axis itself at the same location. The standard STD $k-\varepsilon$ model results in a spreading rate of $dr_{1/2}/dx = 0.075$. This value deviates significantly from that found in the literature using the same STD $k-\varepsilon$ model [10], where the value of the spreading rate was determined to be 0.086. We ascribe this discrepancy to the property of the limiters used in the STD $k-\varepsilon$ model. Due to the coarse grid resolution at the nozzle exit, strong gradients at the jet boundary occur, thereby reducing the accuracy of the adopted numerical scheme. By modifying the value of the constant $C_{1\varepsilon}$ to 1.4 instead of its standard value 1.44, the spreading rate is improved to $dr_{1/2}/dx = 0.08$. Therefore, this modification should be employed whenever the nozzle exit cannot be resolved sufficiently. However, the value of the spreading rate predicted by using the standard value of the constant $C_{1\varepsilon}$ and by implementing the v^2–f and the nonlinear models is nearly about $dr_{1/2}/dx = 0.082$ and 0.086, respectively. This indicates that the problem of varying the model constants could be diminished.

3.2. Impinging jet problem

More recently, impinging jets have received considerable attention because of their widespread engineering and industrial applications. Examples include manufacturing, material processing, cooling of turbine blades and drying paper, textiles, quenching of metals and glass, and more recently cooling of electronic equipment [29]. There are numerous papers dealing with this problem both numerically and experimentally, focusing essentially on the prediction of the heat transfer parameters [30]. However, the prediction of the turbulent characteristics and structure have been investigated less as a result of the complexity associated with the experimental measurements or the numerical challenges.

For a better understanding of the jet impingement heat transfer process, details of the flow and turbulence characteristics and structure are required [31]. Consequently, numerical simulation of the impinging jet problem would have been an important key for quantifying the effect of different parameters of interest. However, many complex features are encountered in the impinging problem due to stagnation, jet entrainment, and high streamline curvature. These features prove to be incompatible with most existing turbulence models, which have essentially been developed and tested for flows parallel to a wall. Therefore, the complexity of such a flow has led to it being chosen as an excellent and challenging test-case for the validation of different turbulence models. The configuration of the impinging jet is shown in Fig. 7;

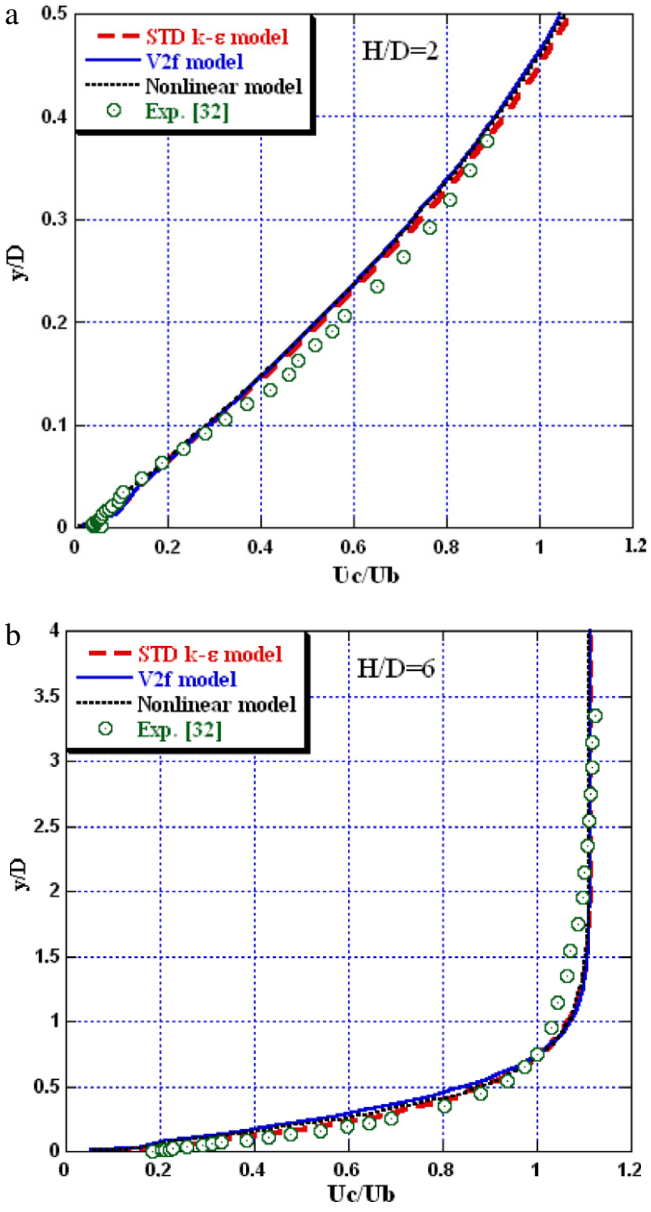

Fig. 8. Axial velocity profiles for the impinging jet problem for $H/D = 2$ (a) and $H/D = 6$ (b); $(r/D = 0)$ at Re = 23 000.

a turbulent air flow issues from a nozzle, with diameter D, and uniform exit velocity U. The problem is governed by the physical, hydrodynamic, and geometrical parameters of the jet/surface system. The principal parameter, in addition to D and U, is the distance between the nozzle and the surface of impact, denoted by H, which is generally expressed in the dimensionless form H/D. Fig. 7 illustrates the present numerical results for the axial velocity contours of an impinging jet for $H/D = 2$ and Re = 23 000.

The boundary conditions are required to be specified on all sides of the computational domain. At the axis of symmetry, the radial velocity component and the gradient of the other dependent variable are equal to zero. Along the solid wall, a no-slip boundary condition is applied for the velocity components, zero value for the turbulent kinetic energy, and zero gradients for the energy dissipation rate. The inlet boundary conditions imposed at the nozzle are described as in the case of turbulent jet (see Section 3.1). Two different values of nozzle to plate distance ($H/D = 2$ and $H/D = 6$) have been considered for Reynolds number equal to 23 000. The corresponding grids used for such dimensions are non-uniform 50 × 80 (for the $H/D = 2$ case) and 150 × 80 (for

the $H/D = 6$ case) grids (y and r dimensions), respectively (see Fig. 7). In the present simulation cases, the effect of grid resolution is also considered to find a suitable grid. However, with further refinements, there is no significant improvement in the results obtained. The experimental data selected to validate the results of the present simulation is a set of flow measurements carried out by [32] using hot-wire measurements.

3.2.1. Axial velocity profiles along the jet axis

The performance of the three selected turbulence models is considered in this section for the impinging jet problem. The centerline velocity profiles on the stagnation line ($r/D = 0$) are shown in Fig. 8 for the two nozzle to wall distances ($H/D = 2$ and $H/D = 6$) at Re $= 23\,000$ and compared with the experimental measurements of [32]. The calculated profiles for the centerline velocity U_c are normalized by the bulk velocity U_b (average velocity over the nozzle cross-sectional area). Fig. 8 shows that there is very little difference between the predictions of the different turbulence models, and quite good agreement with the experimental data is observed as well for the two ratios of H/D considered. Moreover, nearly all turbulence models adopted represent the steep variation of the velocity profile in the near-wall region adequately.

In such a context, it is difficult to assess the performance of the turbulence models by presenting the mean variable profiles. Near the solid boundaries, the implemented wall functions for the STD k–ε model give almost the same axial velocity profile as obtained from the v^2–f model or the nonlinear k–ε model without using any wall functions. Therefore, the assessment of the different turbulence models should be evaluated through the prediction and comparison of the Reynolds stresses.

3.2.2. Streamwise Reynolds stress component

In the present section, only a sample of the numerical results for the Reynolds stresses obtained is presented, to show the performance of the turbulence models considered. Fig. 9 illustrates the development of the axial Reynolds stress profile (predicted at the centerline of the jet) against the dimensionless normal distance from the impinging wall for the two space distances ($H/D = 2$ and $H/D = 6$) at Re $= 23\,000$. The comparison of the numerical results obtained showed that none of the implemented turbulence models perfectly matches the experimental data. However, the nonlinear k–ε model and the v^2–f model give more reliable results than the STD k–ε model, especially in the case of nozzle distance $H/D = 6$.

In the experimental work of [32], not all the Reynolds stress components were presented at the stagnation line. However, other measurements were carried out in the radial direction for different values of r/D. When comparing our numerical results of the Reynolds stresses components at different locations of r/D with the available measurements of [32], the same conclusion was obtained, i.e. none of the turbulence models adopted can be considered as a general one; nevertheless, the mean velocity profiles were reasonably well predicted by all turbulence models. The turbulence models adopted showed either an overestimation or underestimation of the experimental measurements for the different stresses considered, which makes the final conclusion difficult to draw.

It is expected that the nonlinear model performs consistently better than other linear models as a result of the cubic relation coupling the strain with the vorticity and stress tensors. However, the quantitative comparisons between the numerical results obtained from the nonlinear model and the experimental measurements showed very little difference. Similar results were also demonstrated in [19], where only small differences were observed between the experimental measurements [32] and the profiles of r.m.s. velocities perpendicular and parallel to the wall. Therefore,

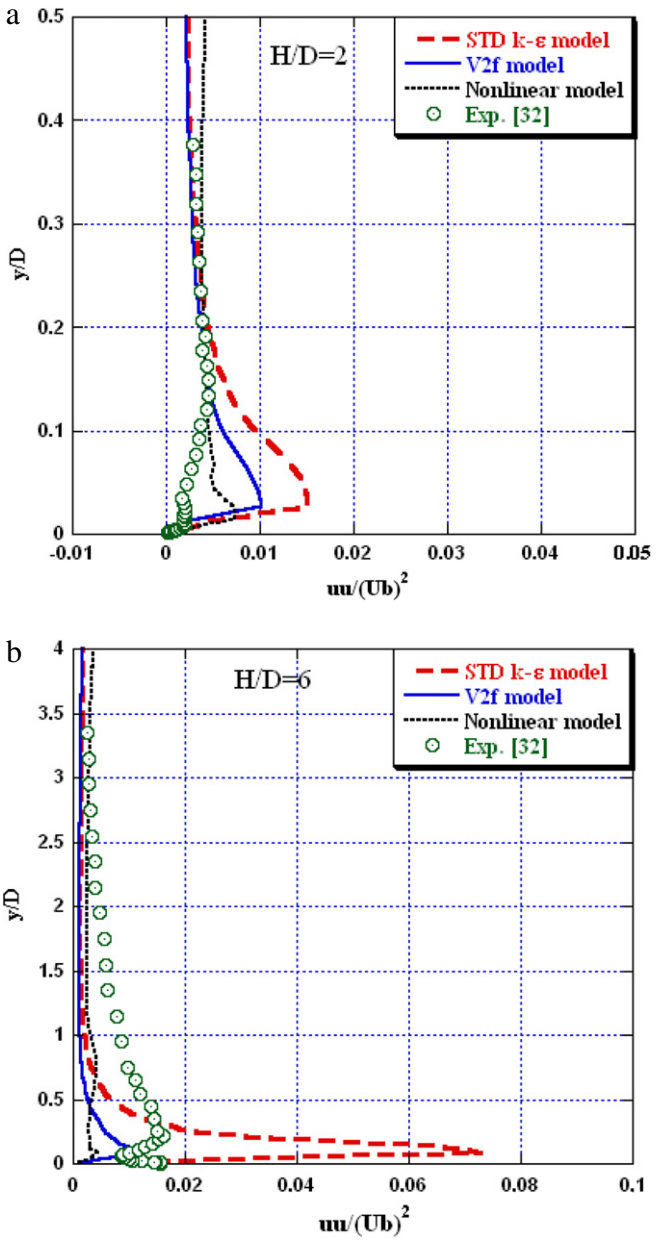

Fig. 9. Axial Reynolds stress profiles for the impinging jet problem at $H/D = 2$ (a) and $H/D = 6$ (b); ($r/D = 0$) at Re $= 23\,000$.

there is no need to duplicate the same results as a matching between the numerical results and the experimental measurements is already expected. However, a slight variation of the associated model coefficients ($C_1, \ldots, C_7$) and the expressions proposed for C_μ and f_μ have shown a significant effect on the final results. This is considered a general problem of either linear or nonlinear turbulence models.

From the above discussion, it is essential to check the validity of these turbulence models using additional criteria, because most of the turbulence models to date are sometimes fitted for a given test-case, and they might give much worse results when they flow conditions are changed. Therefore, the prediction and visualization of the flow structure is believed to play a significant role in evaluating the turbulence model behavior according to the physical characteristics encountered in the specified jet flow applications. The most important predicted parameter in the impinging jet problem is the turbulent viscosity near the stagnation point. This is essentially dependent on the good approximation of the normal stresses at the

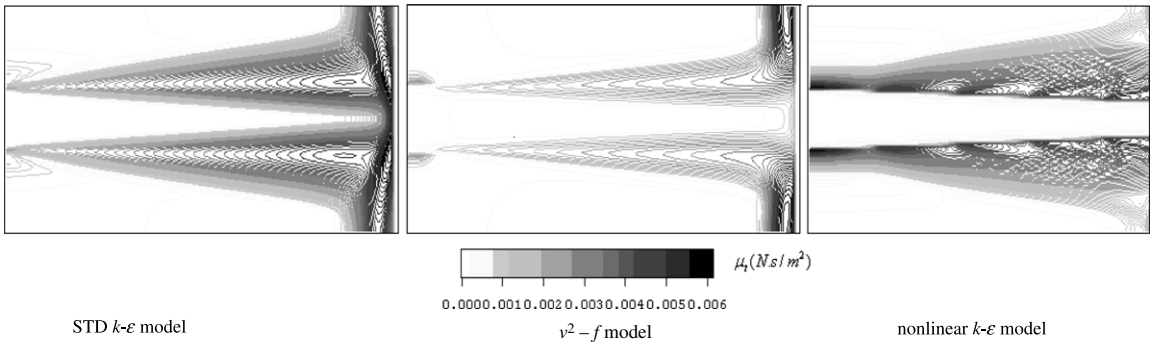

Fig. 10. Turbulent viscosity structures for the impinging jet problem for $H/D = 6$ and Re $= 23\,000$ (comparison of the turbulence models used).

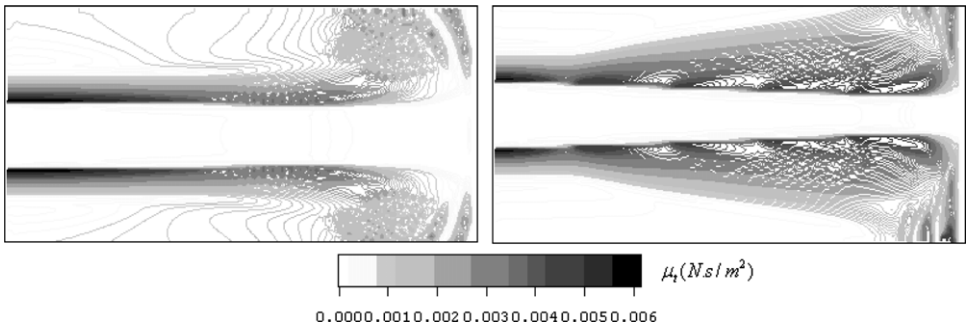

Fig. 11. Turbulent viscosity structures for the impinging jet problem computed from the nonlinear turbulence model for $H/D = 2$ (left) and $H/D = 6$ (right) at Re $= 23\,000$.

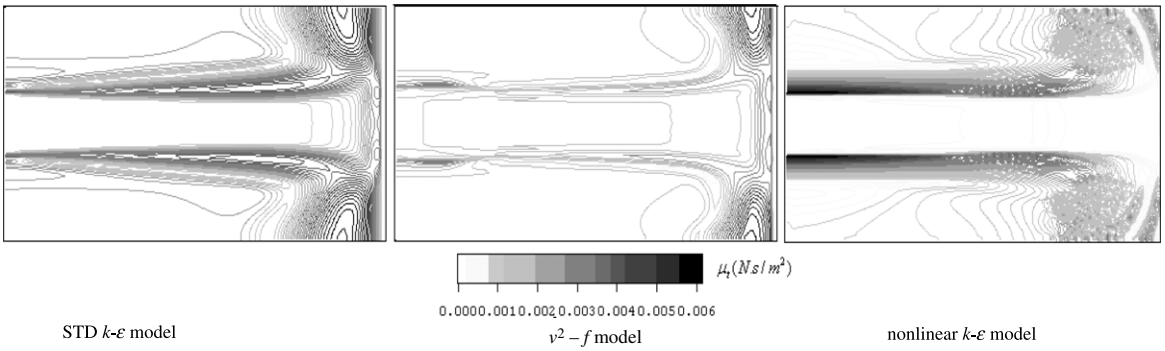

Fig. 12. Turbulent viscosity structures for the impinging jet problem for $H/D = 2$ and Re $= 23\,000$ (comparison of the turbulence models used).

stagnation point and the constitutive relation adopted in representing the stress–strain relation of the selected turbulence model. The nonlinear relation applied in the nonlinear model is developed essentially to match the anisotropic stresses and the streamline curvature effects. Both effects are encountered in impinging jet problems. Consequently, in the following sections, the turbulent viscosity structure and the stagnation pressure are numerically predicted and visualized from the different linear and nonlinear turbulence models adopted and compared with each other to indicate the capability of each turbulence model in predicting the physical phenomena of the impinging jet problem.

3.2.3. Turbulent viscosity structure

In order to show the effectiveness of the selected group of turbulence models, the structure of the turbulent viscosity is illustrated in Fig. 10 for the nozzle to wall distance $H/D = 6$ and Re $= 23\,000$. The STD k–ε model shows an excessive generation of turbulent viscosity near the stagnation point. This can be attributed to the misrepresentation of the turbulent kinetic energy production rate. This problem is observed much less when using the v^2–f model, and almost disappears on using the nonlinear representation of the Reynolds stress components through the application of the nonlinear model.

An important feature of the turbulent viscosity structure is shown in Fig. 11 when comparing the numerical results of the nonlinear k–ε model when $H/D = 2$ and $H/D = 6$ for Re $=$ $23\,000$. For smaller nozzle to wall distance, i.e. $H/D = 2$, the evolution of the issued jet is not complete. The incoming jet hits the wall in a wider area than that observed for $H/D = 6$, and the reflecting flow is characterized by a highly disturbed eddy structure on both sides of the stagnation line of the impinging jet. Because of the rapid impinging process and the small nozzle to wall distance, an extreme jet momentum is produced, resulting in a group of curved streamlines that evolve after the impinging process. This behavior of the streamline curvature makes most of the experimental measurements in such a region very complex and less accurate. However, for larger nozzle to wall distance, i.e. $H/D = 6$, the incoming jet is considered to be fully expanded regarding sufficient impinging distance compared with the initial mixing axial distance required for complete jet evolution, which can extend to an x/D value of about 5 [33]. Consequently, and due to the nearly complete jet evolution, the impinging jet moves

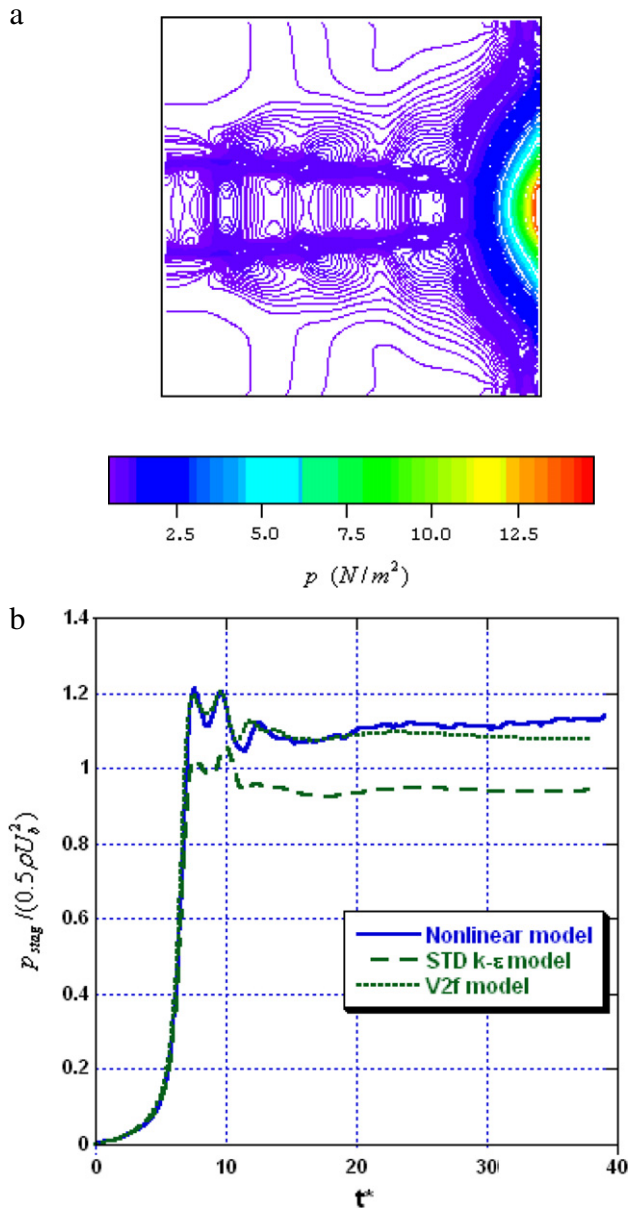

Fig. 13. Pressure contours (a) and transient stagnation pressure (b) for the impinging jet problem for $H/D = 6$ and Re $= 23\,000$.

nearly parallel to the wall after the impinging process. It should be pointed out that, by using the nonlinear model, no excessive generation of the turbulent viscosity in the stagnation point could be observed in both cases ($H/D = 2$ and $H/D = 6$).

It should also be pointed out that the highly disturbed eddy structure obtained for $H/D = 2$ by using the nonlinear k–ε model could not be sufficiently well predicted using the other linear models, as illustrated in Fig. 12. The success of the nonlinear k–ε model in predicting the turbulent viscosity structure is much better than that of the other models, based on the Boussinesq concept. This reveals that nonlinear models are more suitable for predicting the realistic features of the impinging jet problem. However, the group of coefficients implemented in such models needs to be validated over a wide range of numerical simulations as well as experimental measurements in similar applications in order to obtain good quantitative results. This problem might be considered in more detail in our future research.

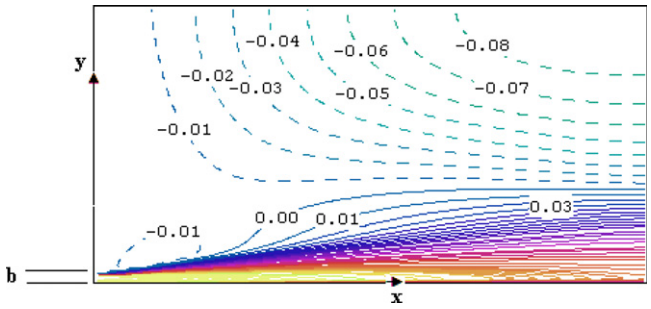

Fig. 14. Steady-state streamwise velocity contours of a plane turbulent wall jet (present simulation for Re $= 13\,974$).

3.2.4. Stagnation pressure

An important problem in the impinging process is the development of stagnation pressure with time at the impinging point, i.e. at $r/D = 0$. The accurate prediction of the mean pressure level at the impinging point has a significant effect on the estimation of the resulting force on the considered structure (wall or bluff body). This may be considered a challenging problem in fluid–structure interaction applications. Consequently, in the following figures, a numerical prediction for the transient pressure value and its behavior by using the implemented linear and nonlinear turbulence models has been carried out.

Fig. 13(a) shows the pressure contours in the computational domain, while Fig. 13(b) illustrates the history of the stagnation pressure until the steady-state value starting from atmospheric initial conditions, scaled with the nozzle-exit dynamic pressure, for the specified case ($H/D = 6$ and Reynolds number $= 23\,000$). The pressure contours (computed from the nonlinear model) indicate the prediction of maximum pressure value at the stagnation point with an acoustic field ahead of the impinging plane. This acoustic field may be useful in studying the generated sound phenomenon due to the jet impinging processes. The important feature of the stagnation pressure for the considered case (developed impinging jet) is that it reaches a maximum value in a short time, followed by a fluctuation period until a nearly constant value is achieved; see Fig. 13(b). In Fig. 13(b), P_{stag} is the stagnation pressure and t^* is the nondimensional time, defined as $t^* = t \times U_b/H$. The maximum values of the steady-state stagnation pressure are affected by the considered turbulence model in such a manner that the nonlinear model and the v^2–f model overpredict the value obtained from the STD k–ε model. This could be a consequence of the excessive generation of the production term developed by the STD k–ε model at the stagnation point, which leads to incorrect prediction of the stagnation pressure value. This associated problem can be less viewed by using the nonlinear model or the v^2–f model, which are more useful for jet impinging applications.

In general, the stagnation-pressure levels as well as the radial distribution of turbulent pressure characteristics on the impinging surface have been rather poorly documented in the literature; therefore, more investigations are required for a better understanding of the fluctuation behavior and the transition from the impingement region to the developed radial wall jet region.

3.3. Plane turbulent wall jet

In the present section, the numerical method developed here along with the selected turbulence models is applied further to predict the plane turbulent wall jet flow. A turbulent wall jet is essentially obtained by issuing a fluid at high velocity along a smooth or rough boundary. The complexity of such flow is a consequence of the strong interaction of the inner wall boundary

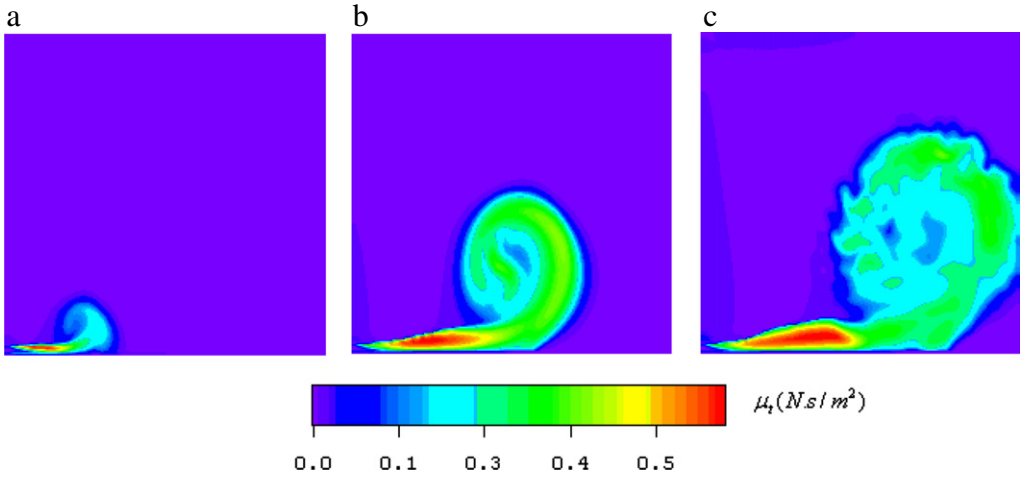

Fig. 15. The transient evolution of turbulent viscosity at different time intervals for the wall jet problem using the nonlinear turbulence model.

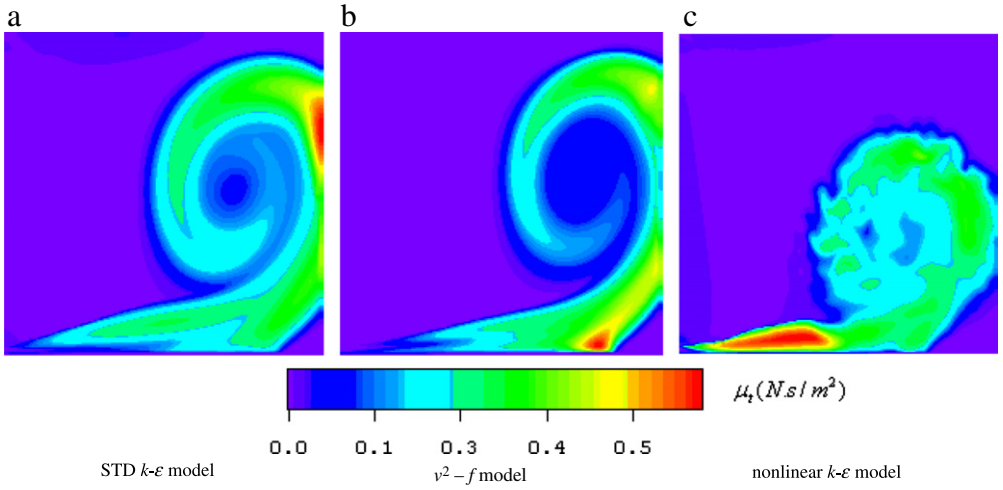

Fig. 16. The turbulent viscosity structure at the same time as predicted by the different adopted turbulence models.

layer and the outer free jet. In the inner boundary layer, the flow velocity increases from zero at the wall to a local maximum, while the jet velocity decreases from a local maximum to zero. This strong interaction poses challenging problems for the associated numerical modeling of the wall jet problem, which can be seen in many industrial applications such as solid smoothing and film cooling of gas turbine blades. Such a type of flow has been widely investigated both experimentally or numerically; see e.g. [34–37]. However, the spreading mechanism of the wall jet, which affects the velocity distribution and, consequently, the associated related characteristics, is not well understood.

In general, and from a review of the literature, it was concluded that the high lateral rate of spread can be attributed to stress-induced axial vorticity, which is generated by the anisotropy of the Reynolds normal stresses perpendicular to the jet axis; for more details see [38]. Therefore, the correct prediction of the remarkable lateral spreading rate of a wall jet depends on the accurate modeling of the Reynolds normal stresses. As we restrict our developed numerical method to the prediction of a two-dimensional plane turbulent wall jet, consequently, only the experimental verification of the numerically obtained Reynolds stresses is presented. It should be pointed out that most of the previous numerical results are concerned with a two-dimensional laminar wall jet or three-dimensional turbulent wall jet. Accordingly, the presentation of Reynolds stresses in the case of a two-dimensional turbulent wall jet is rarely found in the literature.

The plane turbulent jet simulated in the numerical experiment reported here, as shown in Fig. 14, was modified to closely match the boundary conditions of the experimental work of [35]. A water jet is discharged from a two-dimensional slot having a height $b = 9.6$ mm. A flat mean velocity profile is assumed at the inlet of the slot with a mean velocity of 1 m/s, which gives an inlet Reynolds number of 9600. The inflow turbulence kinetic energy is uniformly considered as a function of the inlet turbulence intensity, which is taken to be 0.003.

The computational grid employed and tested for the plane turbulent wall jet problem consists of 173 (streamwise, x) by 173 (vertical, y) grid cells for a computational domain dimension of 2.16×1.2 m^2, respectively. Three types of boundary condition are applied to describe the flow field within the computational domain, namely inlet boundary conditions at the slot exit, no-slip boundary conditions for the left and south walls, and outlet boundary conditions at the top and the right side of the computational domain. The numerical solution is started from zero initial values for all variables in the computational domain. The flow field is developed in time until it reaches a statistically steady-state condition where the final results are obtained.

Before the presentation of the statistically steady-state results of the plane turbulent wall jet, a sample of the transient evolution for the turbulent viscosity (eddy) structure predicted by the adopted nonlinear turbulence models is presented in Fig. 15. The numerical visualization of the turbulent viscosity in the previous

figure reveals the formation of the coherent (eddy) structure at later time intervals Fig. 15(c), which could be predicted by the present two-dimensional RANS simulation using the nonlinear turbulence model. This is considered a capability of nonlinear models as a result of the nonlinear constitutive relation.

In comparison with the other turbulence models considered, shown in Fig. 16, this coherent structure is not predicted by the linear models, either the k–ε model or the v^2–f model. Also, the turbulent viscosity predicted by the nonlinear turbulence model shows a maximum in the inner boundary layer along the wall, while a minimum value of the turbulent viscosity has been predicted by the linear models in the inner boundary layer region. This can also be considered a limitation of linear turbulence models in such applications. The reduction of turbulent viscosity estimated from the linear model may be due to the increased predicted dissipation rate, and hence the turbulence energy decreases in such a region.

3.3.1. Mean velocity profiles

The numerically predicted mean velocity profiles, obtained by the various turbulence models selected, are compared at different axial locations with the experimental measurements of [35], where LDV was used. It should be pointed that the experimental measurements in [35] have an uncertainty in measuring the slot height and the spanwise velocity distribution of approximately ± 0.1 mm and $\pm 0.25\%$, respectively.

Fig. 17 shows the comparison of the mean velocity profiles scaled by the maximum velocity in the vertical direction at two different positions, $x/b = 70$ (Fig. 17(a)) and 150 (Fig. 17(b)). The vertical distance is scaled with the distance $y_{1/2}$, at which the half of the maximum velocity occurs (as represented in the original paper [35]).

The velocity comparisons at two different axial locations show that the nonlinear model gives the best agreement with the experimental measurements, especially in the near-wall region. This could be a consequence of the correct prediction of the turbulent stresses that are the essential parameters in calculating the turbulent kinetic energy production and dissipation rates. This of course leads to an adequate computation of the turbulent viscosity, especially in the inner region, as shown in Fig. 16.

3.3.2. Reynolds stresses profiles

The turbulent quantities predicted from the different selected turbulence models are compared with the experimental measurements of [35]. Fig. 18 shows the distributions of the Reynolds stress components uu (Fig. 18(a)), uv (Fig. 18(b)) and vv (Fig. 18(c)), normalized by the square of the local maximum velocity and plotted against the nondimensional distance $y/y_{1/2}$ at an axial distance $x/b = 70$. It can be shown that the nonlinear turbulence model gives the best agreement with the experimental measurements compared with the other linear turbulence models. The adequate prediction of the near-wall region using the nonlinear model is clearly visible, especially for the Reynolds stress components uu and uv, as can be seen in Fig. 18(a) and (b), respectively. The negative peak of turbulent shear stress near the wall as seen in Fig. 18(b) is overpredicted by both linear models; however, a lesser degree can be seen from the nonlinear turbulence model. Moreover, the linear turbulence models show a large deviation from the experimental measurements in the outer shear layer; in contrast, the nonlinear turbulence model gives only small discrepancies from the measured values in the outer region of the wall jet. In general, the well-predicted inner and outer wall jet regions from the nonlinear turbulence model adopted show the remarkable ability of such a turbulence model in wall jet applications.

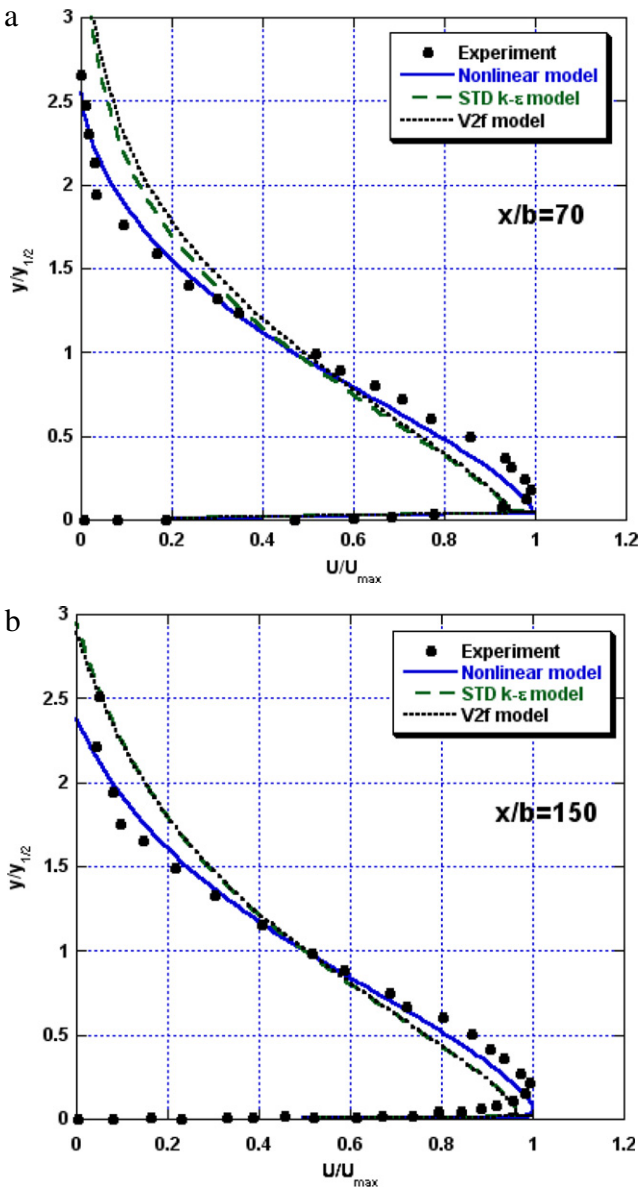

Fig. 17. Comparison of the mean velocity profiles of a wall jet with experimental measurements [35] at $x/b = 70$ (a) and $x/b = 150$ (b).

Conclusion

The performance of three selected k–ε based turbulence models has been investigated numerically. The turbulence models selected are the STD k–ε, v^2–f and the cubic nonlinear k–ε models. They have been validated against three different jet applications, namely a free round jet, the impinging jet problem, and the wall jet problem. The numerical prediction of the turbulent flow considered is obtained by solving the unsteady RANS equations on a non-staggered grid system by using the control volume approach. A quantitative comparison of the predicted numerical results with the experimental measurements reveals that a fairly good agreement has been obtained for the mean velocity profiles for almost all selected turbulence models. The linear turbulence models are found to give better predictions than the nonlinear models in simple (non-impinging) jet flow. However, the linear turbulence model, in comparison with the nonlinear turbulence model, gave a lesser degree of agreement with the experimental measurements when comparing the Reynolds stress components in impinging jet problems. Moreover, the turbulent viscosity

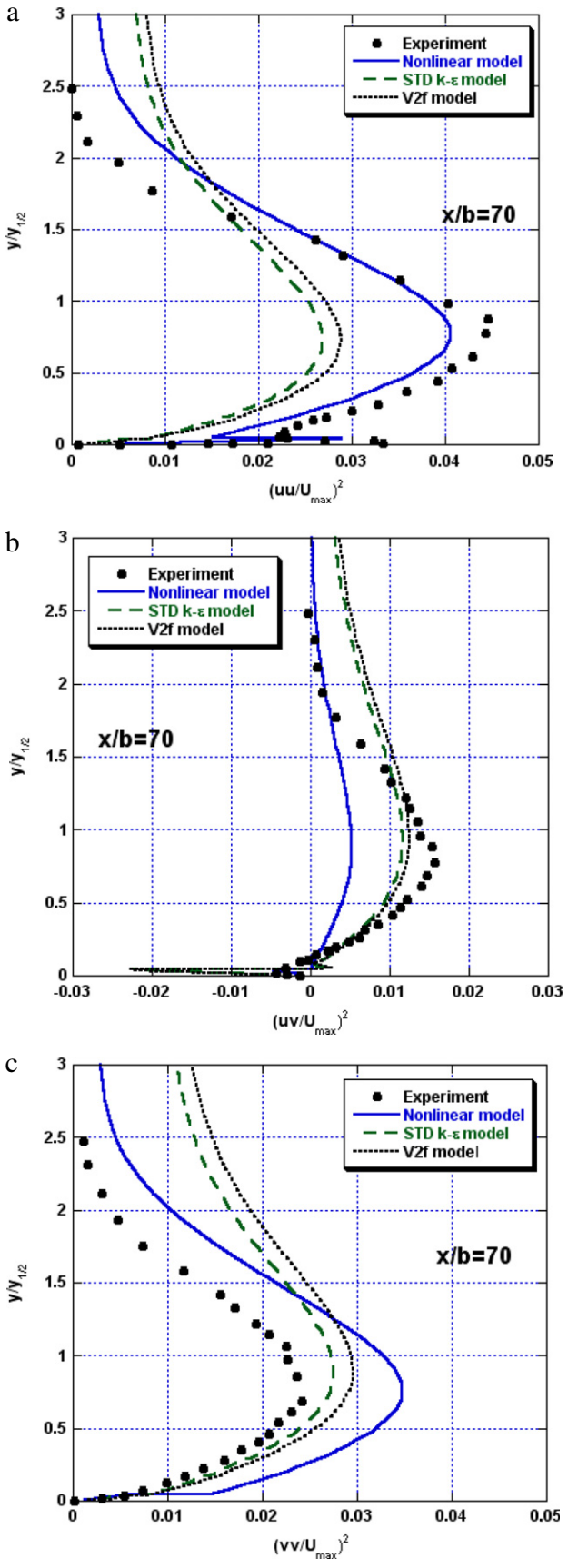

Fig. 18. Comparison of the Reynolds stresses components of a wall jet with experimental measurements [35].

structure predicted by the nonlinear turbulence model can be seen to be more realistic than that predicted by the linear turbulence models. All these important results can be attributed to the nonlinear constitutive relations presented in the nonlinear model and the model constants included. The quality of the solution of the nonlinear models is significantly affected by the constant values which were estimated to give the best agreement with the experimental measurements in the case of the impinging jet problem. However, for other simple jet flows, these constants gave significantly worse results in comparison with the standard k–ε results.

It should be pointed out that the prediction of the turbulent viscosity structure is as important as the prediction of the mean turbulence properties. Therefore, the best turbulence model should predict both turbulent characteristics (mean turbulent variables and turbulent viscosity structure) adequately. Accordingly, among the different selected turbulence models, the nonlinear model is chosen to be the most reliable turbulence model in impinging and wall jet applications, as it predicts the mean turbulent variables and the associated turbulent viscosity structure in an accurate manner.

References

[1] M. Frage, N.K.R. Kevlahan, V. Perrier, K. Schneider, in: J.C. Van der Berg (Ed.), Turbulence Analysis Modeling and Computing Using Wavelets, Cambridge Univ. Press, Cambridge, 1999.
[2] W.P. Jones, B.E. Launder, The prediction of laminarization with a two-equation models of turbulence, Int. J. Heat Mass Transfer 15 (2) (1972) 301–314.
[3] P.R. Spalart, Detached eddy simulation 1997–2000, Fluid Mech. Appl. 65 (5) (2004) 235–237.
[4] D.E. Goldstein, O.V. Vasilyev, N.K.R. Kevlahan, CVS and SCALES simulation of 3D isotropic turbulence, J. Turbul. 6 (37) (2005) 1–20.
[5] T.J. Craft, B.E. Launder, On the spreading mechanism of the three-dimensional turbulent wall jet, J. Fluid Mech. 435 (2001) 305–326.
[6] B.E. Launder, D.B. Spalding, The numerical computation of turbulent flows, Internat. J. Numer. Methods Fluids 15 (1974) 127–146.
[7] W. Rodi, Turbulence models and their application in hydraulics, in: State of the Art Paper, Presented by IAHR-Section on Fundamentals of Division II: Exp. and Math. Fluid Dynamics, 1979.
[8] W. Rodi, N. Mansour, Low Reynolds number $k-\varepsilon$ modeling with the aid of direct simulation data, J. Fluid Mech. 250 (1993) 509–529.
[9] M. Behnia, S. Parneix, Y. Shabbany, P.A. Durbin, Numerical study of turbulent heat transfer in confined and unconfined impinging jets, Int. J. Heat Fluid Flow 20 (1999) 1–9.
[10] D.C. Wilcox, Turbulence Modelling for CFD, DCW Industries Inc., La Canada, CA, USA, 1993.
[11] X. Zhou, Z. Sun, F. Durst, G. Brenner, Numerical simulation of turbulent jet flow and combustion, Comput. Math. Appl. 38 (1999) 179–191.
[12] N.R. Panchapakesan, J.L. Lumley, Turbulence measurements in axisymmetric jets of air and helium. Part 1. Air jet, J. Fluid Mech. 246 (1993) 197–223.
[13] V. Yakhot, S.A. Orzag, Renormalization group analysis of turbulence. I. Basic theory, J. Sci. Comput. 1 (1986) 3–51.
[14] K. Hanjalic, R.E. Launder, Contribution towards a Reynolds-stress closure for low-Reynolds-number turbulence, J. Fluid Mech. 74 (1976) 593–610.
[15] V.C. Patel, W. Rodi, W. Scheurer, Turbulence models for near-wall and low Reynolds number flows: a review, AIAA J. 23 (1985) 1308–1319.
[16] B.E. Launder, Low Reynolds number turbulence near walls, Rept. TFD/86/4, Univ. of Manchester, England, UK, 1986.
[17] P.A. Durbin, Application of a near-wall turbulence model to boundary layers and heat transfer, Int. J. Heat Fluid Flow 14 (4) (1993) 316–323.
[18] P.A. Durbin, Separated flow computations with the k–ε–v^2 model, AIAA J. 33 (4) (1995) 659–664.
[19] T.J. Craft, B.E. Launder, K. Suga, Development and application of a cubic eddy-viscosity model of turbulence, Int. J. Heat Fluid Flow 17 (1996) 108–115.
[20] D.D. Apsley, W.L. Chen, M.A. Leschziner, F.S. Lien, Nonlinear eddy viscosity modeling of separated flows, J. Hydraul. Res. 35 (1997) 723–748.
[21] W.A. El-Askary, A. Balabel, Prediction of reattachment turbulent shear flow in asymmetric divergent channel using linear and non-linear turbulence models, Eng. Res. J. Fac. Eng. Menoufiya Univ. 30 (4) (2007) 535–550.
[22] F.S. Lien, G. Kalitzin, Computations of transonic flow with the v^2–f turbulence model, Int. J. Heat Fluid Flow 22 (2001) 53–61.
[23] S.V. Patankar, Numerical Heat Transfer and Fluid Flow, Hemisphere Publishing Corporation, 1980.
[24] A. Balabel, RANS modeling of gas jet impinging onto a deformable liquid interface, Emirates J. Eng. Res. 13 (1) (2007) 1–13.
[25] J.P. Bonnet, R.D. Moser, W. Rodi, Free shear flow. In a selection of test cases for the validation of LES of turbulent flows, AGARD Adv. Rep. 345 (1998) 29–36 (Chapter 6).
[26] I. Wygnanski, H. Fiedler, Some measurements in the self-preserving jet, J. Fluid Mech. 38 (3) (1969) 577–612.

[27] A.A. Townsend, The Structure of Turbulent Shear Flow, second ed., Cambridge University Press, 1976.
[28] H. Hussein, S. Capp, W. George, Velocity measurements in a high-Reynolds-number, momentum-conserving, axisymmetric, turbulent jet, J. Fluid Mech. 258 (1994) 31–75.
[29] A.H. Beitelmal, M.A. Saad, C.D. Patel, The effect of inclination on the heat transfer between a flat surface and an impinging two-dimensional air jet, Int. J. Heat Fluid Flow 21 (2000) 156–163.
[30] Y. Chung, K. Luo, Unsteady heat transfer analysis of an impinging jet, J. Heat Transfer 124 (2002) 1039–1048.
[31] K. Jambunathan, E. Lai, M. Moss, B. Button, A review of heat transfer data for single circular jet impingement, Int. J. Heat Fluid Flow 13 (2) (1992) 106–115.
[32] D. Cooper, B.L. Jackson, G. Liao, Impinging jet studies for turbulence model assessment. I. Flow-field experiments, Int. J. Heat Mass Transfer 36 (1993) 2675–2684.
[33] D.A. Anderson, C.J. Tannehill, R.H. Pletcher, Computational Fluid Mechanics and Heat Transfer, Heimsphere Publishing Corporation, 1984.
[34] X.K. Wang, S.K. Tan, Experimental investigation of the interaction between a plane wall jet and parallel offset jet, Exp. Fluids 42 (2007) 551–562.
[35] J.G. Eriksson, R.I. Karlsson, J. Persson, An experimental study of a two-dimensional plane turbulent wall jet, Exp. Fluids 25 (1998) 50–60.
[36] J. Kechiche, H.A. Mhiri, G. Le Palec, P. Bournot, Application of low Reynolds number $k - \varepsilon$ turbulence models to the study of turbulent wall jets, Int. J. Thermal Sci. 43 (2004) 201–211.
[37] S. Aloysius, L.C. Wrobel, Comparison of flow and dispersion properties of free and wall turbulent jets for source dynamics characterisation, Environ. Modell. Softw. 24 (2009) 926–937.
[38] H.M. Lübcke, Th. Rung, F. Thiele, Prediction of the spreading mechanism of 3D turbulent wall jets with explicit Reynolds-stress closure, Int. J. Heat Fluid Flow 24 (2003) 434–443.